Mesophase and size manipulation of itraconazole liquid crystalline nanoparticles produced via quasi nanoemulsion precipitation

Naila A. Mugheirbi and Lidia Tajber*

School of Pharmacy and Pharmaceutical Sciences, Trinity College Dublin, Dublin 2, Ireland.

*To whom correspondence should be addressed: lidia.tajber@tcd.ie,

Phone: 00353 1 896 2787 Fax: 00353 1 896 2810

Abstract

The fabrication of drug nanoparticles (NPs) with process-mediated tunable properties and performances continues to grow rapidly during the last decades. This study investigates the synthesis and phase tuning of nanoparticulate itraconazole (ITR) mesophases using quasi nanoemulsion precipitation from acetone/water systems to seek out an alternative pathway to the nucleation-based NP formation. ITR liquid crystalline (LC) phases were formed and nematic-smectic mesomorphism was achieved via controlling solvent:antisolvent temperature difference ($\Delta T_{S:AS}$). The use of $\Delta T_{S:AS}$=49.5 °C was associated with a nematic assembly, while intercalated smectic A layering was observed at $\Delta T_{S:AS}$=0 °C, with both phases confined in the nanospheres at room temperature. The quasi emulsion system has not been investigated at the nanoscale before and in contrary to the microscale, quasi nanoemulsion was observed over the solvent:antisolvent viscosity ratios of 1:7 to 1:1.4. Poly(acrylic acid) in the solvent phase exhibited a concentration dependent interaction when ITR formed NPs. This nanodroplet-based approach enabled the preparation of a stable ITR nanodispersion using Poloxamer 407 at 80 °C, which was unachievable before using precipitation via nucleation. Findings of this work lay groundwork in terms of rationalised molecular assembly as a tool in designing pharmaceutical LC NPs with tailored properties.

Keywords: Itraconazole, Liquid crystal, Quasi nanoemulsion, Nematic, Smectic, Poloxamer 407.

1. Introduction

The advances in drug design have led to a radical change in the development of active pharmaceutical ingredients (APIs), however at a price of dramatically decreasing their biorelevant properties, mainly solubility. Those APIs are estimated to constitute 40% of the currently developed potential drugs, where low bioavailability is the undesirable consequence of the poor solubility. Nanotechnology has been established as a promising pathway to enhance dissolution and solubility of such substances [1]. Itraconazole is an anti-infective drug that suffers from the above drawbacks, however some attempts involving fabrication in the nanoscale have been found to boost its bioavailability [2, 3].

While a few reports on amorphous and crystalline ITR nanoparticles (NPs) can be found in literature, liquid crystalline ITR NPs and, in general, liquid crystalline drug NPs were overlooked [4]. A liquid crystals (LC) is an intermediate state between the crystalline and amorphous states with a combination of residual order and mobility thus known as mesophases [5]. APIs in the LC form have been reported to possess enhanced solubility in comparison to their crystalline counterparts [6]. Almost all types of supramolecular interactions, including van der Walls interaction, hydrogen bonds and π-π interactions, can be observed in LCs [7]. Molecules capable of forming mesophases are known as mesogens and can be classified according to the anisotropy of their shape into rod-like and disc-like [8] with the former exhibiting the highest molecular anisotropy. Thus nanosized liquid crystals possess the combinatorial effect of the nanomaterials' large surface area, the compromised molecular order of mesophases, which is expected to enhance solubility and dissolution, and advantageous stability on comparison to amorphous due to lower Gibbs free energy [9].

ITR molecule is highly anisotropic with a rod like structure (Figure 1). Nematic and smectic liquid crystalline phases of ITR were previously achieved via controlled cooling of melted crystals [5, 10]. However, a nematic phase can easily be misinterpreted as isotropic (amorphous) using X-ray diffraction due to similarity in diffraction patterns of both phases.

Here, we report on tuning the LC phase in ITR NPs through controlling the quasi nano-emulsion precipitation process parameters, especially the solvent to antisolvent temperature

difference ($\Delta T_{S:AS}$). The $\Delta T_{S:AS}$ transpired to be a critical parameter associated with the nematic or smectic assembly with both phases, to our surprise, confined in the shell of nanospheres at room temperature which, to the best of our knowledge, has not been demonstrated before. The underlying mechanism of ITR NP formation was investigated and the impact of $\Delta T_{S:AS}$, the solvent:antisolvent viscosity ratio (ρ) and functional properties, such as miscibility and possibility of interactions, of the included polymer on the properties of the formed particles were examined. Different polymers were tested including poly(acrylic acid) (PAA), cellulose acetate phthalate (CAP) and Poloxamer 407 (P407), although the focus is mainly on P407 as it demonstrated the capability to markedly improve ITR dissolution [11, 12]. The formation of ITR-P407 NPs at elevated temperature adds to the unique achievements of this work since it was reported to be infeasible before [13].

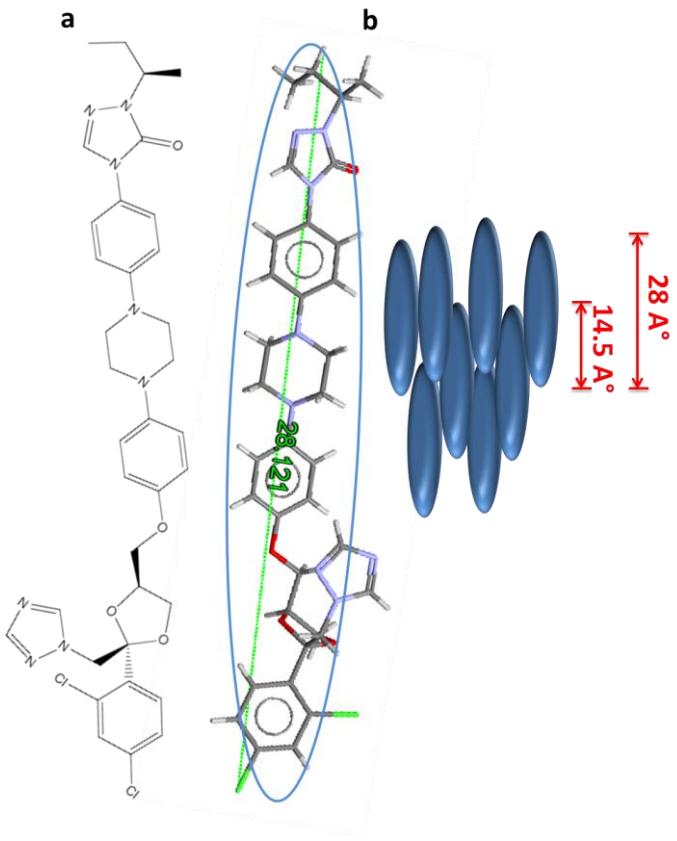

Figure 1. (a) Chemical structure of ITR (ChemBioDraw). (b) Schematic illustration of ITR molecule (Mercury® 3.5.1) with the molecular arrangement and interplanar spacing in the intercalated smectic A phase.

2. Materials and Methods

2.1. Materials

Itraconazole (ITR) was a gift from Neuland Laboratories Ltd. (Welding, Hamburg, Germany). Poloxamer 407 (poly(ethylene glycol)-block-poly(propylene glycol)-block-poly(ethylene glycol), P407) was purchased from BASF Corp. (Ludwigshafen, Germany). Acetone Chromasolv® HPLC grade was obtained from Sigma-Aldrich (Dorset, UK), while acetonitrile HPLC grade was purchased from Fisher Scientific (Loughborough, UK). Poly(acrylic acid) (PAA), as Carbopol 981 was obtained from BFGoodrich (Brecksville, OH, USA). Ethanol (≥99.8%), employed in DVS experiments and cellulose acetate phthalate (CAP) were acquired from Sigma-Aldrich (Dublin, Ireland). All other chemicals were of analytical grade and used as supplied.

2.2. Methods

2.2.1. Determination of solubility of crystalline ITR

The solubility of crystalline ITR in acetone at 50 °C in the presence of P407 at different concentrations (1, 2, 3 and 4 mg/ml) was determined using a high performance liquid chromatography (HPLC) method as carried out before [4].

2.2.2. Preparation of ITR NPs

ITR NPs were prepared as previously described [4] with some modifications and details of experimental conditions are presented in Table 1. The modifications included changing the temperature of the antisolvent phase (water), thus creating a temperature gradient ($\Delta T_{S:AS}$). Solvent was acetone. PAA was used to tune the viscosity of the antisolvent phase. CAP was determined to be miscible with ITR based on calculated theoretical miscibility using Flory-Huggins interaction parameters [14].

Table 1. Summary of the precipitation conditions and properties of NPs produced. The solvent:antisolvent (S:AS) v/v ratio was 1:10 in all experiments [4] and the solvent phase was kept at 50 °C. T- temperature, $\Delta T_{S:AS}$ – temperature difference between solvent (S) and antisolvent (AS), ITR – itraconazole, P407 – Pluronic 407, CAP - cellulose acetate phthalate, PAA - poly(acrylic acid) (as Carbopol).

Sample	T_{AS} (°C)	$\Delta T_{S:AS}$ (°C)	ITR Concentration (mg/ml)	Polymer concentration in S phase (mg/ml)		Polymer concentration in AS phase (mg/ml)
				P407	CAP	PAA
F1	0.5	49.5	6.4	0	0	0
F2	0.5	49.5	7.9	1	0	0
F3	50	0	6.4	0	0	0
F4	50	0	7.9	1	0	0
F5	80	30	6.4	0	0	0
F6	80	30	7.9	1	0	0
F7	80	30	6.4	0	1	0
F8	80	30	6.4	0	0	0.033
F9	80	30	6.4	0	0	0.05
F10	80	30	6.4	0	0	0.1
F11	80	30	7.9	1	0	0.033
F12	80	30	6.4	0	1	0.033

2.2.3. Dynamic light scattering (DLS) and zeta potential (ZP)

The mean particle size and the polydispersity indices of NPs were measured using a Zetasizer Nano ZS series (Malvern Instruments, UK). The dispersions were placed in DTS1061 clear disposable zeta cells. All measurements were carried out at 25 °C with an equilibration time of 2 min. The analysis was performed in triplicate for each sample and the mean particle diameter along with the polydispersity index were recorded and corrected for viscosity of the continuous phase. Electrophoretic mobility values were measured by laser Doppler velocimetry (LDV) using DTS1061 cells and were converted to zeta potential values. Average zeta potential values of at least three batches were calculated and corrected for viscosity of the continuous phase [15].

2.2.4. Residual acetone quantification

The residual acetone content in the continuous phase of ITR NP dispersions was determined by measuring ZP values of the 200 nm Nanosphere® standard (Malvern

Instruments, UK) dispersed in acetone/water mixtures with varying acetone v/v ratios. A calibration curve (Figure 1S) was constructed by plotting the ZP values of mixtures containing 10 µl the Nanosphere® standard dispersed in 500 µl of acetone/water mixtures against the acetone/water v/v ratio.

ITR dispersions prepared at the investigated $\Delta T_{S:AS}$ were filtered using 0.1 µm filters (Sartorius Stedim, Germany). An aliquot of 500 µl of the filtrate was mixed with 10 µl of the Nanosphere® standard and the measured ZP values were used to calculate the acetone content using the calibration curve constructed earlier.

2.2.5. NP morphology

2.2.5.1. Scanning electron microscopy (SEM)

A Zeiss Supra variable pressure field emission scanning electron microscope (Germany) equipped with a secondary electron detector and accelerating voltage of 5kV was used for the morphological examination of ITR nanoparticles. Aliquots of the ITR nanodispersions were placed on a silicon chip 5*7 mm with (111) orientation, fixed on aluminium stubs and dried using nitrogen purge. For the samples collected after dynamic vapour sorption (DVS) experiments, powders were placed on carbon tabs fitted on aluminium stubs. All samples were sputter coated with gold-palladium under vacuum before analysis.

2.2.5.2. Transmission electron microscopy

Transmission electron microscopy (TEM) characterisation of the NPs prepared using a different temperature of the antisolvent phase (0.5, 50 and 80 °C) was carried out to investigate the effect of ΔT on the thickness of shell of the NPs formed. TEM imaging was performed on a TEM Titan instrument (FEI Ltd, Hillsboro, OR). Centrifuged residues of ITR NPs were redispersed in water and mounted on Cu holey carbon-coated TEM grids and imaged at 300 kV.

2.2.6. Elucidation of the mechanism of NP formation

2.2.6.1. Viscosity measurements

A Vibro viscometer SV-10 (A&D Ltd., Japan) was used to measure the viscosity of deionised water and pure acetone at different temperatures employed in the precipitation studies. Each

sample was subjected to a heating ramp to the required temperature using a thermostated water jacket followed by cooling to 0.5 °C. The average of the recorded viscosity values in the heating and cooling cycles at each temperature was used. The impact of the 1 mg/ml P407 and 1 mg/ml CAP on the viscosity of acetone was also studied using the same method. Similarly, a change in water viscosity at 80 °C upon the addition of different PAA concentrations was measured.

2.2.6.2. Visualisation of the Tyndall effect

The Tyndall effect, at the investigated temperatures, in a glass vial was examined before and after the injection of 0.1 ml acetone to 1 ml water as reported before [16].

2.2.6.3. Investigation of micelle formation at 1 mg/ml P407

DLS was utilised to investigate if 1 mg/ml P407 is able to form micelles at the employed antisolvent temperatures. For this experiment, deionised water was ultrasonically degased for 10 min using a F15053 Fisherbrand sonicator (Elma, Germany). The degased water was used to prepare 1 mg/ml P407 solution, the solution was filtered using a 0.1 µm membrane filter (Sartorius Stedim, Germany) and placed in a PCS8501 glass cuvette. The solution was heated *in situ* in a Zetasizer Nano ZS series and size measurements were performed at 25, 50 and 80 °C.

2.2.7. Wide angle powder X-ray diffraction (WAXS) and small angle powder X-ray diffraction (SAXS)

WAXS measurements were performed over a 2θ range of 5-35° [4]. Peak positioning and d-spacing measurements were performed using PDXL comprehensive analysis software (Rigaku, Japan). SAXS studies were performed using a Bruker D8 Discover with a monochromatic copper Kα1 source. Scanning with 666 s/point with effective 0.1 mm slits was applied [17].

2.2.8. Differential scanning calorimetry (DSC)

A range of crystalline ITR/P407 physical mixtures prepared in different w/w ratios were examined by DSC [4] and data were used to construct a calibration curve to quantify the P407 content in the NPs (Figure 2S). For the purpose of P407 quantification, the samples were

heated in an oven (Memmert U10, Germany) at 40 °C following dynamic vapour sorption analysis with ethanol to remove any remaining solvent. The dried samples were then subjected to DSC scans as described above and the enthalpy of P407 melting was used to quantify the P407 content.

2.2.9. Attenuated total reflection Fourier transform infra-red spectroscopy (ATR-FTIR)

Infrared spectra were recorded on a PerkinElmer Spectrum One FT-IR Spectrometer and evaluated using Spectrum v5.0.1 software. Each spectrum was scanned in the range of 650–4000 cm^{-1} with a resolution of 4 cm^{-1} and minimum of four scans were collected and averaged in order to obtain good quality spectra. The spectra were normalised and background corrected using the following base points: 690, 909, 1307, 1596, 1780, 2507, 3029 and 4000 cm^{-1}. A second derivative, using the Savizky–Golay algorithm with seven smoothing points, were calculated for each absorbance spectrum.

2.2.10. Determination of change in the degree of disorder by dynamic vapour sorption (DVS)

Freeze dried ITR NPs were subjected to DVS analysis as previously described [4]. Second sorption cycle isotherms were also determined where absence of a mass loss indicated full crystallisation. The complete crystallisation was further confirmed using WAXS and DSC. The change in the degree of disorder in samples produced using different $\Delta T_{S:AS}$ compared to when $\Delta T_{S:AS}$ =0 °C was determined using Eq. (1),

$$\% \text{ increase in disorder} = 100 \times \frac{\Delta m \times ms}{md} \times \frac{1}{\Delta m_{\Delta t=0}} \quad \text{Eq. 1}$$

where ∆m is the difference in the mass uptake (%) of the ITR NPs between the first and second sorption cycles at a system specific p/p_0, *ms* is the sample mass in the DVS, *md* is the mass of the ITR in the overall sample mass, and $\Delta m_{\Delta t=0}$ is the difference in mass uptake between the first and second sorption cycles of the NPs precipitated when $\Delta T_{S:AS}$= 0 °C.

2.2.11. Statistical analysis

Statistical analyses were performed via one way ANOVA with the Tukey comparison test, as specified in relevant sections, using Minitab Release 16. For all tests, $p \leq 0.05$ was used as the criterion to assess statistical significance.

2.2.12. Computational investigations

The full interaction map (FIM) for itraconazole (CSD refcode TEHZIP) was generated using Mercury 3.5.1 software. The carbonyl oxygen, C-Cl and aromatic C-H were used as the hydrogen bond (H-bond) acceptors, halogen bond and hydrophobic interactions probes, respectively. The propensities, a numerical representation of how much more likely an interaction is at a certain contour with respect to random chance [18], for the propped interactions along with the hotspots and short contacts were calculated.

3. Results and Discussion

3.1. Investigations into the formulation and process variables leading to ITR NPs

In an effort to bridge the gap between pharmaceutical nanotechnology and pharmaceutical liquid crystals, the impact of process parameter manipulation on the size and the mesophase of ITR NPs was probed. As a starting point, the effects of antisolvent temperature (T_{AS}) and polymer concentration in the solvent or antisolvent phase on the formation of NPs was investigated (Table 1) followed by solid state characterisation and computational investigation. While an increase in ITR solubility with an increase in P407 concentration was observed, no complex formation between the two species in acetone was determined when the Higuchi and Connors relationship was applied [19]. Higher concentrations of P407 in acetone (2, 3 and 4 mg/ml) resulted in the formation of NPs, however some of the produced NPs converted into more stable crystalline microparticles (Figure 3S), thus in this work we have only focused on the 1 mg/ml P407 systems. SE micrographs (Figure 2) and hydrodynamic diameters (Figure 3a) indicated that discrete NPs were formed for all formulations apart for F1, where aggregates with sizes of 521±3 nm of particles smaller than 100 nm can be seen (Figure 2a).

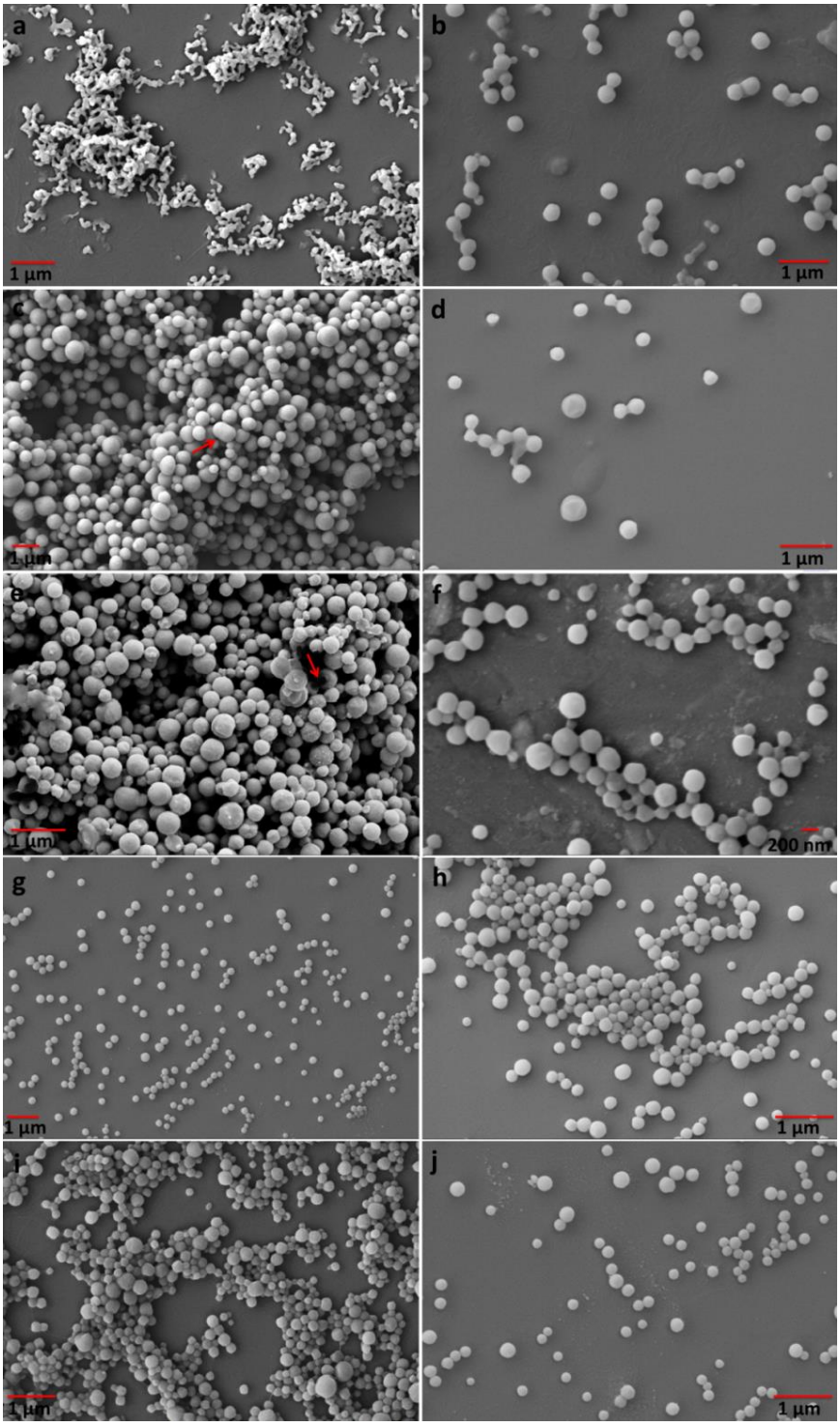

Figure 2. Scanning electron micrographs of (a) F1 nano-aggregates, (b) F2, (c) F3 with a deformed but non broken particle indicated by red arrow, (d) F4 (e) F5 showing hollow particle indicated by red arrow, (f) F6, (g) F7 with apparent homogenous size, (h) F8, (i) F11 and (j) F12 ITR NPs.

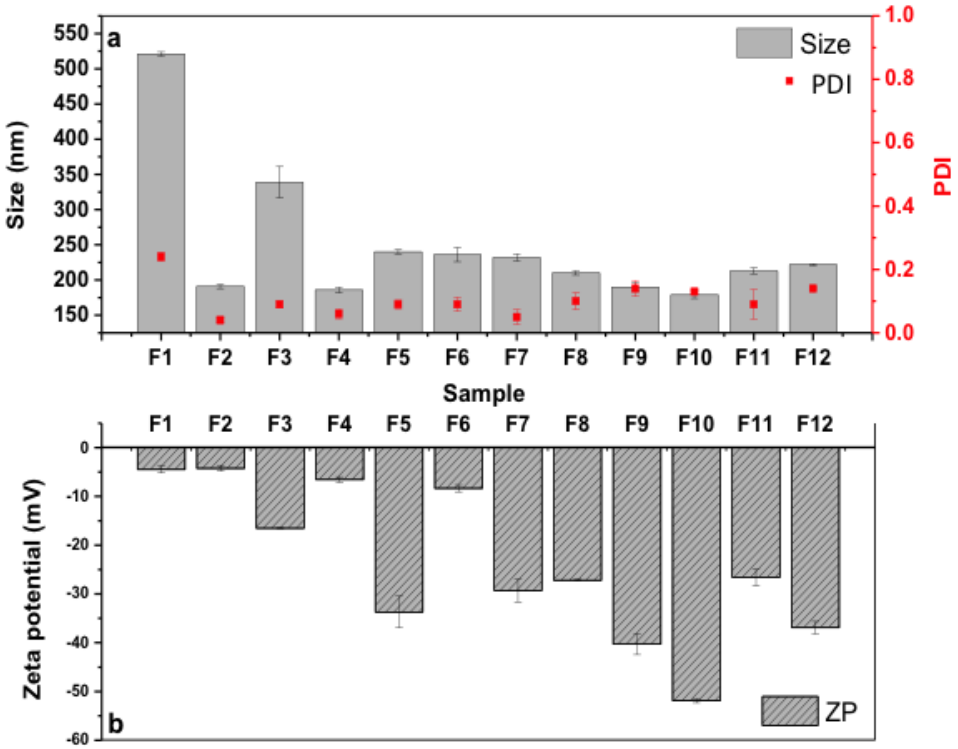

Figure 3. (a) Hydrodynamic particle size (grey bars) and polydispersity index (PDI, red squares) and (b) Zeta potential values (grey hashed bars) of samples F1 to F12.

Increasing viscosity of the antisolvent phase via the addition of PAA (F8) resulted in the production of smaller particles compared to F5 as can be inferred from the SEM micrographs (Figure 2h). The inclusion of 1 mg/ml CAP (F7), an ITR miscible polymer, in the solvent phase resulted in the formation of NPs with the same apparent morphology as their polymer free counterparts (F5). The low polydispersity index (PDI, Figure 3a) of those particles was confirmed by the high homogeneity of size as displayed in the SE micrograph (Figure 2g). Increasing viscosity of the antisolvent phase by the addition of 0.033 mg/ml PAA (system F12) resulted in the formation of smaller particles with greater polydispersity compared to F7. For P407, DLS investigation revealed that 1 mg/ml is below the critical micelle concentration (CMC) at the applied experimental conditions thus the micellar effect on NPs formation was ruled out.

The stabiliser-free NPs formed at 80 °C ($\Delta T_{S:AS}$=30 °C, F5) did not fully redisperse in water following freeze drying. The relatively highly negative zeta potential (ZP) value

(-33.7±3.2 mV, Figure 3b) indicates that NPs in this dispersion are electrostatically stabilised, which explains the poor redispersiblity in water [20, 21]. In contrast, the surfactant nature of P407 suggests the presence of this polymer as a layer on the particle surface leading to a less negative ZP value for F6. This layer sterically stabilise the NPs and shield their surface charge, which explains their good redispersibility in water [22]. The ZP value of ITR NPs prepared when the AS temperature was 50 °C ($\Delta T_{S:AS}$=0 °C, F3) was -16.5±0.6 mV, greater than -33.7±3.2 mV of F5. The residual content of acetone in the AS phase was 6% v/v and this is expected to affect the solvation shell around the particles [23]. The presence of acetone is believed to promote Ostwald ripening, where smaller particles dissolve and deposit on larger particles to achieve a more thermodynamically stable system [24]. Incorporation of P407 (F4) shifted the ZP to -6.5±0.6 mV, when compared to F3. Despite the low negative charge on those particles, steric repulsion is expected to play a role in their stabilisation. For the sample fabricated using the AS phase at 0.5 °C ($\Delta T_{S:AS}$=49.5 °C, F1), the surface charge was very low with the acetone content of 9% v/v in the AS phase. It also can be noted that the ZP values with and without P407 (F1 and F2, respectively) were comparable. This can be attributed to the fact that without the inclusion of a stabiliser nanoaggregates, which are expected to possess lower surface charge [25], were formed rather than discrete NPs.

The inclusion of PAA in the AS phase appeared to have a concentration-based effect on the particle size and ZP as can be seen in Figure 3b. The use of 0.033 mg/ml aqueous solution of PAA (F8) was found to result in a shift in ZP from -33.7±3.2 mV in F5 to -27.2±0.2 mV in F8, which was inconsistent with literature where PAA was found to render the surface of NPs more negative [26].

A DSC scan of F8 (Figure 4a) revealed an increase in the glass transition (Tg) of ITR from 60 to 62 °C using med-point approach, which suggests the presence of considerable miscibility between ITR and PAA at the used concentration.

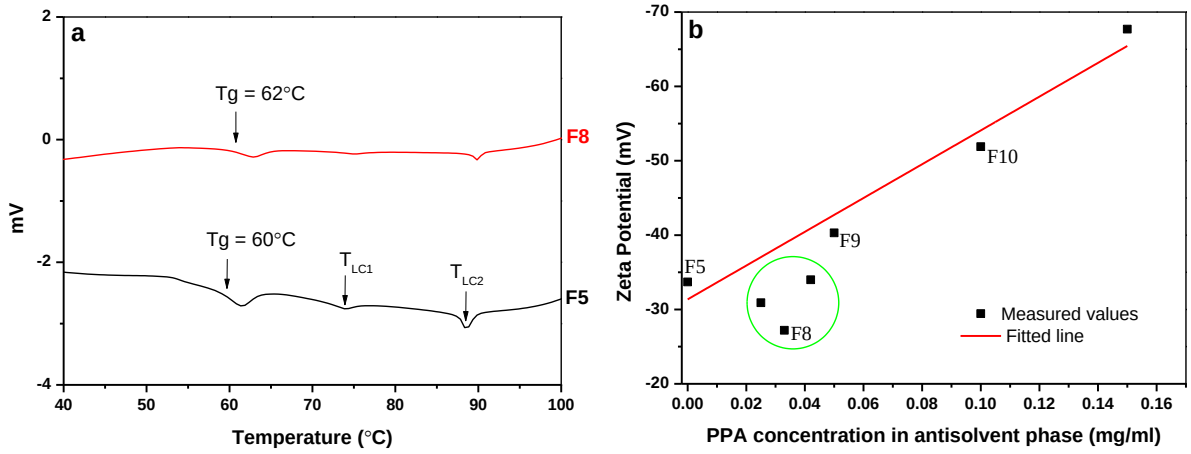

Figure 4. (a) DSC thermograms of F5 and F8; T_g – glass transition, T_{LC1} and T_{LC2} – the first and second endothermic (liquid crystalline) transition, respectively. The T_g shifted from 60 to 62 °C upon the inclusion of 0.033 mg/ml PPA. (b) Zeta potential values of ITR NPs as a function of PAA concentration in the AS phase with the outliers enclosed in the green circle.

Additionally, one of the endothermal (liquid crystalline) transitions (T_{LC1}) in ITR originally located at 74°C [4] was almost invisible which indicates that the observed increase in Tg influenced the ability of ITR to undergo smectic A transition. This influence is most likely due to interaction of ITR with PAA owing to the acidic nature of the polymer and the presence of basic nitrogen atoms in ITR. The use of higher PAA concentrations (0.05 mg/ml in F9 and 0.1 mg/ml in F10) resulted in shifting the ZP towards more negative values (-40.3±2.2 and -51.9±0.4 mV, respectively) compared to F8, which is an indication of concentration dependent miscibility of components in NPs. To further investigate the correlation between the PAA concentration in the AS phase and ZP, three additional dispersions made using the following concentration of PAA in water were examined, 0.025, 0.042 and 0.15 mg/ml, which had the following ZP values: -30.9±0.2, -34±0.1 and -67.7±2.76 mV, respectively. Figure 4b shows the outliers, at low PAA concentrations, for which deviations of ZP values were determined. The inclusion of CAP, a polymer that is miscible with ITR, had a similar effect on ZP to the low PAA concentration (F8).

NPs obtained using a combination of 1 mg/ml P407 in the solvent phase and 0.033 mg/ml PAA in the AS phase (F11) had a comparable ZP value to F8 NPs. In contrast, when CAP was combined with 0.033 mg/ml PAA (F12), more negatively charged ITR NPs, compared to F8, were produced, which could be due to the favourable interaction of ITR with CAP where the cellulose-based backbone [27] shields ITR from interaction with PAA, which in turn contributes to the shift of ZP towards more negative values.

3.2. Internal structure of ITR NPs

Figure 5 shows the TE micrographs of resultant NPs using different AS temperature. It is clear that the investigated particles were hollow. The effect of $\Delta T_{S:AS}$ on the shell diameter is illustrated with the thickest crust of about 120 nm achieved when $\Delta T_{S:AS}$=0 °C (F3, Figure 5b). With large $\Delta T_{S:AS}$, the shell thickness decreases significantly, where $\Delta T_{S:AS}$=30 °C was associated with around 30 nm NP shell with a blowhole (indicated by the red arrow in Figure 5c, which is consistent with SE micrograph in Figure 2e). The $\Delta T_{S:AS}$=49.5 °C (F1) resulted in the formation of smaller particles/aggregates with the shell thickness of around 15 nm as shown in Figure 5a presenting a particle with a blowhole (red arrow).

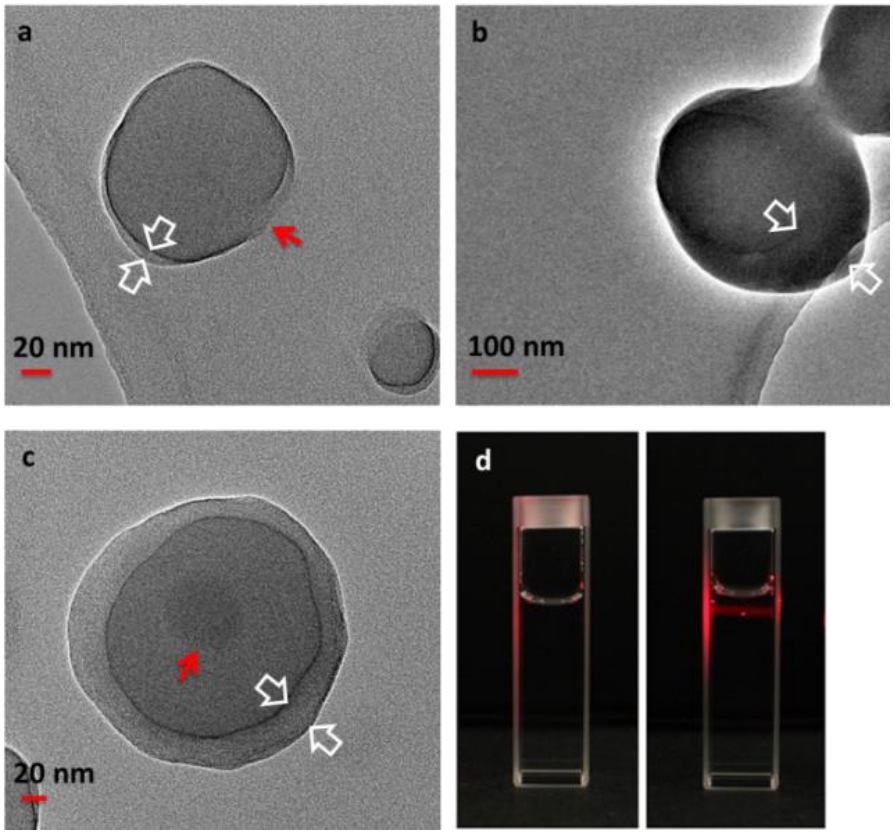

Figure 5. TEM images of a NP in (a) F1 with 15 nm thick shell and a blowhole (red arrow), (b) F3 showing the thickest shell of 120 nm and (c) F5 with a blowhole (red arrow) and 30 nm thick shell, and (d) Laser light scattering in pure water (left) and acetone:water 1:10 v/v mixture (right), 30 seconds after the addition of acetone to pure water. The Tyndall effect is clearly visible as the red pathway of laser light in the liquid.

3.3. Mechanism of NP formation

Quasi emulsion solvent diffusion (QESD) precipitation using the acetone-water system has been used in the past for the spherical crystallisation of drug substances to improve their performance during formulation processes [28, 29, 30, 31, 32]. Nevertheless, to the best of our knowledge, NPs formation using QESD has not been reported before. The hypothesis is that ITR NPs are formed via solidification of droplets through counter-diffusion of solvent and antisolvent following the break up stage, which is confirmed by the hollow structure of the particles (Figure 5). The breakup of those droplets is controlled by deformation, which can be described using the Taylor's equation [33]:

$$D = \frac{G\alpha\mu}{\gamma}\left[\frac{19\rho+16}{16\rho+16}\right] \quad \text{Eq.2}$$

where D - deformation of drop, G - shear rate, α - radius of liquid droplet, μ - viscosity of the continuous phase, ρ - viscosity ratio (μ'/μ) where μ' is viscosity of the solvent (dispersed) phase and γ - interfacial tension. The higher the D value, the easier the droplet breaks up.

To investigate the applicability of this mechanism to the systems at the nanoscale, a viscosity ratio between the solvent to antisolvent (ρ) was determined for each condition investigated (Table 1S). For water at 0.5 °C, the ρ is 1:7. This ratio changed with an increase in the antisolvent phase temperature to 1:2 and 1:1.4 for the AS phase at 50 and 80 °C, respectively. Statistical analysis (ANOVA, $p \leq 0.05$) revealed that the viscosity values of pure acetone and the 1 mg/ml P407 solution in acetone were not significantly different. Therefore, the change in ρ upon the addition of 1 mg/ml P407 to acetone can be considered negligible. The addition of PAA to water at 80 °C was found to decrease ρ, compared to F5, to 1:1.7,

1:2 and 1:2.5 for 0.033, 0.05 and 0.1 mg/ml PAA, respectively. The Tyndall effect was observed in all systems for which the viscosity ratios were calculated (an example is shown in Figure 5d) confirming the generation of liquid segregation in the range of viscosity ratios (ρ) 1:7 to 1:1.4. These values are in agreement with those suggested by Karam et al. for a series of silicone fluids and PEGs [33], however are inconsistent with those reported by Wang et al. for some polymorphic pharmaceuticals [16, 34]. This discrepancy shows that the viscosity ratios necessary to form a quasi-emulsion are system specific and as described by Taylor's equation (eqn 2), droplet deformation occurs due to the interactive effect of various parameters including interfacial tension, shear rate and droplet radius.

Increasing viscosity of the antisolvent phase due to the addition of PAA (F8) resulted in the production of smaller particles compared to F5, which obeys the Taylor's equation. Furthermore, DLS data shows that the higher the concentration of PAA, the smaller the particle size of the precipitated NPs. Meanwhile, the higher the PAA concentration, the greater the PDI values (Figure 3a), which is also demonstrated in the SE micrographs. The polydispersed NPs can be explained by the non-uniform breakage of some droplets into smaller entities due to the relatively high viscosity ratio as reported for oil droplets before [33], which results in a range of sizes formed. A combination of the high viscosity effect of PAA with the surfactant effect of P407 at 80 °C (Figure 2i, sample F11) did not result in any statistically significant impact on the particle size nor PDI (size = 213±4 nm and PDI = 0.09±0.05) when compared to F8.

Collectively, DLS, SEM and TEM data indicated a $\Delta T_{S:AS}$ dependent particle size of NPs with and without P407. Without the surfactant, an increase in the particle size with a decrease in $\Delta T_{S:AS}$ was noticed, where the largest particles (338±21 nm by DLS) were obtained for $\Delta T_{S:AS}$=0 °C. Temperature was reported to have no effect on size of particles in the microscale [32], while it does herein by affecting the viscosity ratio. According to Taylor's equation (Eq. 2), during the precipitation of F3 (T_{AS}=50 °C) without the addition of P407, interfacial tension is expected to be higher than that when P407 was employed, which results in a low D value and thus the formation of large droplets. Those large droplets cannot

be further broken easily through deformation into smaller drops. Additionally, if deformation had occurred particles could have started the solidification process as it can clearly be seen in the SE micrograph (red arrow in Figure 2c) showing deformed but non-broken, solidified, peanut-shaped particles. That is to say, the interfacial tension effect dominates the viscosity ratio effect. In contrast, when a surface active agent such as P407 was included in the solvent phase (F4), smaller particles were observed (Figure 2d) even though the polymer has a negligible effect on viscosity. The ease of droplets breakage by lowering the interfacial tension was reported before [33]. Decreasing the interfacial tension facilitates the breakage of droplets into smaller globules with the aid of the high viscosity of the antisolvent phase at 0.5 °C in F2 compared to F1.

The shell thickness of the formed particles and the presence of particle rupture is determined by $\Delta T_{S:AS}$. Heat transfer is reported to be semi-instantaneous, while mass transfer is the limiting step as it continues for longer following the heat transfer [35] and this leads to the continuation of mass transfer until a thicker crust is formed for the sample made at $\Delta T_{S:AS}$=0 (F3). The effect of $\Delta T_{S:AS}$ is accompanied by the difference in gas solubility in water at different temperatures [36], a parameter disregarded before for the microspheres [32, 37]. When $\Delta T_{S:AS}$=49.5 °C, the addition of the hot solvent to water or aqueous polymer solution results in gas bubbles generation as the net temperature of the mixture increases and consequently gives a rise to particle rupture, observed as blowholes, and terminates the solvent diffusion process. A similar scenario is expected when $\Delta T_{S:AS}$=30 °C, except that the evaporated solvent is responsible for the gas bubbles.

The production of ITR NPs at high temperatures using P407 was not feasible when an ordinary supersaturation-based nucleation process was employed using evaporative precipitation into aqueous solution (EPAS) [13], where an elliptical conical nozzle was used to atomise an organic phase containing ITR and P407 into an aqueous phase at high temperature [38]. According to the authors, in the EPAS process, as the organic solvent evaporates, the formed nuclei are forced to coagulate despite the presence of P407 [13]. In contrast, here, each nanodroplet solidifies as an individual nanoparticle (Figures 2f and 4S),

which then remains dispersed and stabilised by the polymer. Micellar interference is another possible explanation of the failure of the EPAS process to form ITR NPs, while the P407 concentration used herein was below the CMC.

3.4. Evaluation of the phase of matter of ITR NPs

Evaluation of the phase of matter of ITR NPs was accomplished using a group of techniques including wide and small angle X-ray scattering (WAXS and SAXS), as shown in Figure 6, and Fourier transform infra-red spectroscopy (FTIR) (Figure 7).

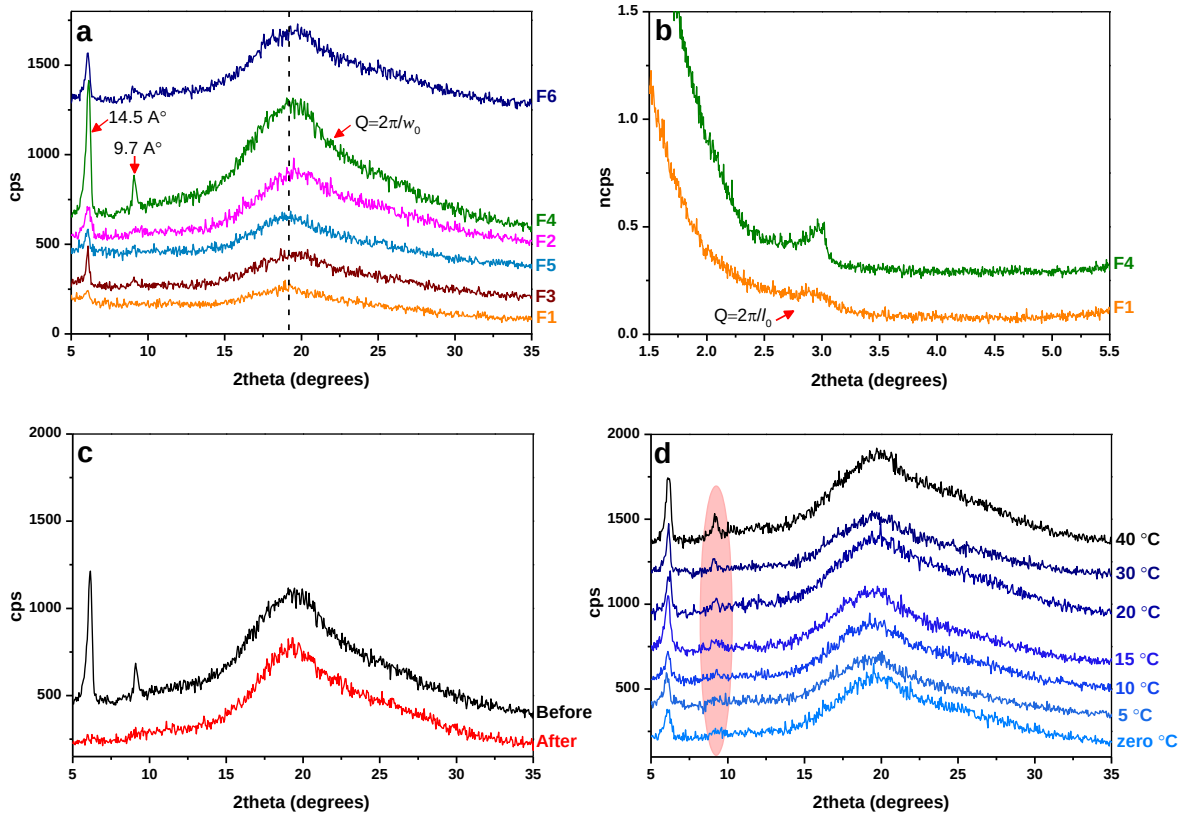

Figure 6. (a) WAXS diffractograms of F1 to F6 illustrating the highest peak intensities in case of F4, (b) SAXS diffractograms of the diffuse maxima at 3° 2θ in F1 and the increase in peak intensity in F4, (c) WAXS diffractograms of F4 before and after DSC scan from 25 to 65°C with both peaks disappeared following the DSC scan, (d) WAXS patterns of ITR NPs precipitated at a series of T_{AS} values zero, 5, 10, 15, 20, 30 and 40 °C highlighting the increase in peak intensity (red background). cps=count per second and ncps=normalised count per second.

A previous X-ray diffraction study of bulk ITR LC phase using CuKα1 source (λ=1.5406 Å) revealed the presence of two diffuse maxima at around 7° and 18° 2θ at 82 °C which was assigned for a chiral nematic phase[10]. Another interesting study using AgKα source (λ= 0.5608 Å) revealed the presence of a diffuse maxima at the low angle region, above and below the LC transition at 89 °C, suggesting the presence of an additional ordering in the sample [39]. The latter cannot be compared with our diffraction patterns as the X-ray source used has a different wavelength to the one used in our study. Moreover, the exact position of that maxima was not specified in the paper.

WAXS patterns of ITR nanoparticles F1-F6, Figure 6a, showed the presence of a characteristic liquid crystal peak at 6.05° 2θ [4] and the absence of characteristic diffraction peaks of the crystalline starting materials, neither ITR nor P407 (Figure 5S). The quasi diffraction peak at 6.05° 2θ corresponds to 14.5 Å interplanar d-spacing and indicates the presence of periodicity or a translational order [40, 41] since orientational order cannot be investigated using X-ray diffraction [42]. In addition to this peak, a second quasi-Bragg peak was observed at 9.05° 2θ in F3, F4 and F6. This peak had the highest intensity when P407 was included in the solvent phase and precipitation performed at 50 °C (F4). The 9.05° 2θ value corresponds to 9.7 Å d-spacing and suggests the presence of additional positional order in the particles precipitated at 50 °C compared to other samples. The occurrence of this peak in ITR, to the best of our knowledge, has not been reported before.

The diffuse maxima in the wide angle position, in the same position described by Six et al [10], were similar in all samples and were in close agreement with the theoretical nematic phase maxima positions. The theoretical position (17° 2θ) was calculated using the formula: $\sin\theta = \frac{Q\lambda}{4\pi}$ where Q is the diffraction vector and for the nematic and smectic phases is estimated to be around $2\pi/w_o$ where w_o is the molecule width. A low angle diffuse peak around 3° 2θ, corresponding to Q of $2\pi/l_o$ where l_o is the molecule length, was observed in F1 and is characteristic of a nematic phase (Figure 6b). The length and width of ITR

molecule are 2.81 and 0.54 nm, respectively as calculated using Mercury® 3.5.1 software (from the crystal structure, CSD code: TEHZIP) which is typical for nematic mesogens [42].

In order to assess whether the peak at 6.05° 2θ is due to the presence of crystalline ITR in the particles or only due to some order in the liquid crystal phase, sample F4 was heated in the DSC furnace to 65 °C, just above the Tg of ITR, and then characterised using WAXS. It was found that the peaks at 6.05° and 9.05° 2θ disappeared (Figure 6c) excluding the presence of crystalline ITR and suggesting *hkl* quasi-planes of 002 and 003, respectively. F4 WAXS pattern, with two pseudo-Brag peaks is typical for one dimensional smectic (Sm) stacking in the thick crust [8, 42]. In addition, the SAXS scan (Figure 6b) illustrates the sharpening of the 3° 2θ peak (*hkl* 001) with interplanar spacing of 28 Å in F4. This equally spaced X-ray diffraction pattern, with Q spacing of $2\pi/d$, is typical of SmA_1 arrangement. The intensity of the 001 quasi-Bragg peak in a perfectly ordered SmA phase is higher than that of the 002 peak, which is not the case here. In contrast, since the highest intensity peak corresponds to layer periodicity close to half the molecule length, intercalated $SmA_{1/2}$ is more likely to exist, facilitated by the curvature strain in the three dimensional spherical shape.

Meanwhile, the hardly visible peak at 6.05 2θ in the F1 diffraction patterns excludes the presence of any layered structure and suggests some lamellar order or localised cybotactic, smectic-like, clusters in the nematic mesophase [42, 43]. The wide angle diffuse peak of the smectic phase was similar to that observed from the nematic phase, indicating that the lateral packing of the molecule remains liquid-like [42]. The existence of the nematic and smectic phases at 25 °C was surprising and has not been reported before. This unusual behaviour can be attributed to the phase confinement in the shell of nanospheres, where reorientation is not feasible at room temperature.

To further assess the effect of $\Delta T_{S:AS}$ on the intensity of the peak at 9.05° 2θ, series of experiments using a range of $\Delta T_{S:AS}$ values, 10, 20, 30, 35, 40 and 45 °C, were carried out and NPs were examined using WAXS (Figure 6d). In all experiments, the solvent phase temperature was kept at 50 °C, while the temperature of the antisolvent phase was varied.

459 The diffractograms of these systems revealed that the 9.05° 2θ peak intensity increased
460 gradually with a decrease in $\Delta T_{S:AS}$ indicating an increase in order.
461 Espitalier et al [35] reported full crystallisation inside ketoprofen quasi-emulsion micro-droplet,
462 which was not observed in ITR NPs with and without polymers in all conditions investigated.
463 This difference can be attributed to the effect of the droplet size (droplet in the nanometer
464 range in this work compared to micrometer-ranged ketoprofen droplets in their work) on the
465 solidification process since nucleation has been reported to be more difficult in smaller drops
466 [44]. Kaminska et al asserted ITR inability to form nematic and smectic phases in binary
467 systems which was found to be possible in our study. ITR weight fraction used in their study
468 was 0.833 while it was 0.95 herein which could be an indication that the formation of LC
469 phases in the binary mixtures is concentration dependent". [45].
470 A further insight into the changes at the molecular level that accompanied the liquid
471 crystalline assembly can be acquired from the full interaction map (FIM), generated based
472 on crystallographic data and infrared spectroscopy (Figure 7). As displayed in Figure 1a,
473 there are no conventional hydrogen bond donating groups in the molecule but a number of
474 available acceptor groups. The FIM of molecule (Figure 7a) illustrates the preferred strength
475 and directionality of interactions of the potential functional group and short contacts. The lack
476 of conventional H-donor groups in the adjacent molecule, to satisfy the H-donor-H-acceptor
477 interaction, suggests that H-bonding is not involved in the formation of either the crystalline
478 or the liquid crystalline forms of ITR. In contrast, the presence of the –CH···π contact and
479 the π···π stacking, which fit the hydrophobic preference contours in the map, is suggested to
480 stabilise the crystalline form and, most likely, the liquid crystalline form. The blue "hotspots"
481 (Figure 7b) indicate the highest propensity for interaction of the C-Cl group with the
482 nucleophilic nitrogen of the triazole ring (13.16) and with the carbonyl oxygen (10.94).
483 Nevertheless, the latter hotspot does not satisfy the preferences for interaction of the
484 nucleophilic carbonyl oxygen in the crystal structure and could be preferred in the
485 intercalated smectic A assembly since it is restricted geometrically in the shell of a
486 nanosphere. It should be also highlighted that the presence of weak halogen bond contacts

(C–Cl···O, between dichlorophenyl and dioxolane groups in a dimeric arrangement) was acknowledged for the first time by Lahtinen et al. [46]. FTIR investigations were focused in the following bands/regions: carbonyl C=O stretching at around 1700 cm^{-1}, asymmetric and symmetric O-C-O stretching at around 1230 and 1147 cm^{-1}, respectively, a 960-1080 cm^{-1} region comprising =C-H out of plane bending and C-N stretching vibrations as well as a 850-920 cm^{-1} region of triazole ring deformations and triazole =C-H out of plane bending absorptions [47]. Considering the various NP formulations, the greatest differences (Figure 7), however only in the triazole, mixed aromatic, C-N and C=O regions, were seen for the sample F4 (T_{AS}=50 °C, with P407) with band shapes resembling those of crystalline ITR. Thus it is logical to assume that this sample had a higher degree of order compared with the rest of NPs, consistent with WAXS data (Figure 6a). Infrared data implies that the part of ITR molecule with the greatest mobility is that containing the triazolone ring.

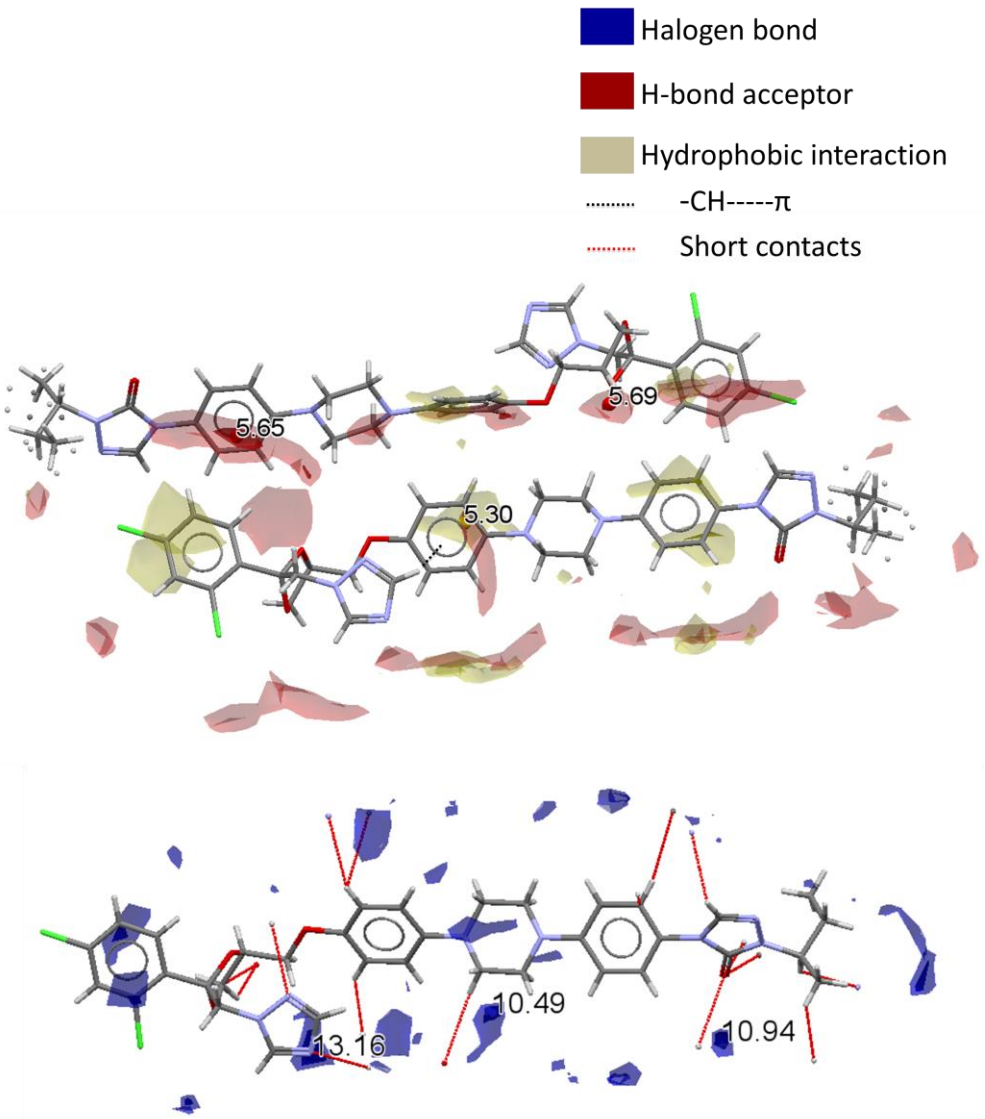
Halogen bond
H-bond acceptor
Hydrophobic interaction
-CH-----π
Short contacts
5.65
5.69
5.30
13.16
10.49
10.94

500 a)

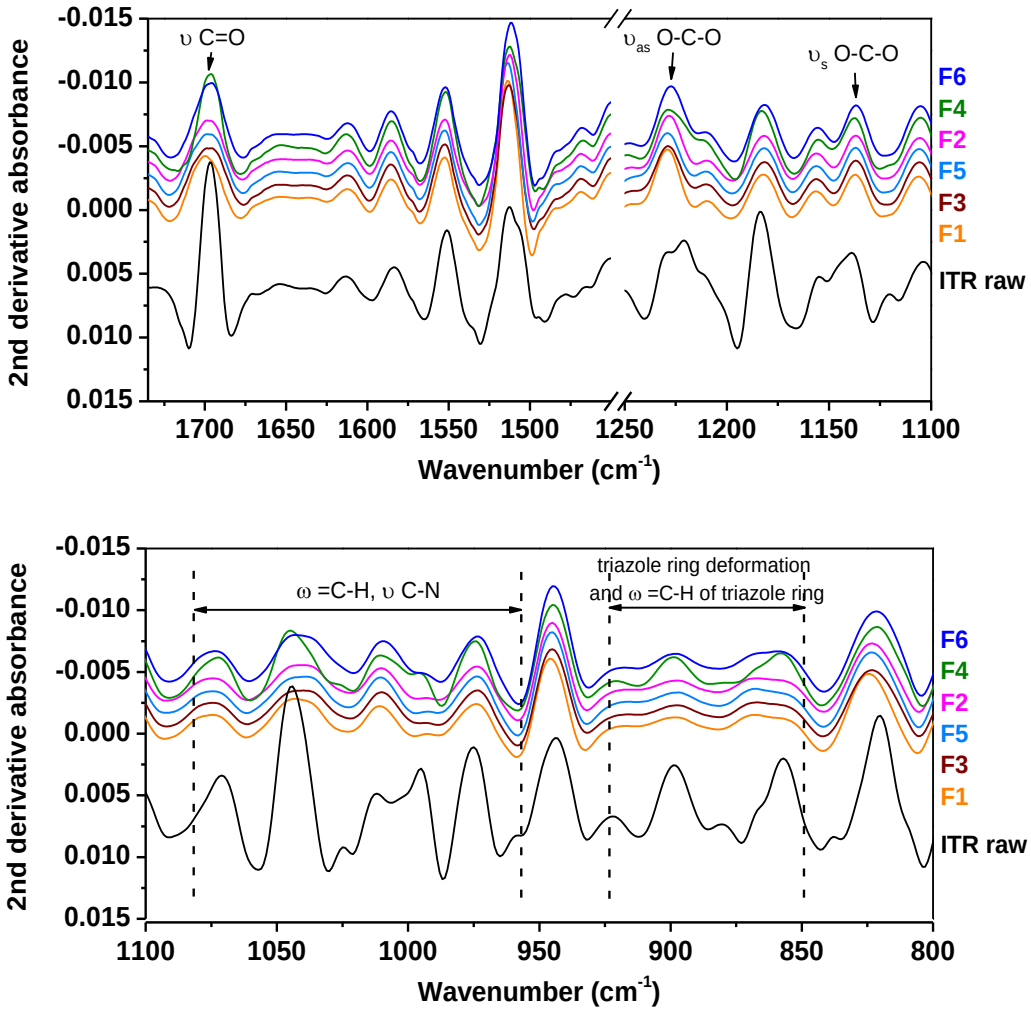

b)

Figure 7. (a) Full interaction map shown around a single ITR molecule in the asymmetric crystal unit (top) and isolated ITR molecule (bottom) with the numerical estimation of propensity for interaction. (b) FTIR analysis (as 2nd derivative of absorbance) of ITR starting material powder (ITR raw) and F1 to F6. ω- out of plane bending, υ - stretching, υ_{as} - asymmetric stretching and υ_s -symmetric stretching.

The sorption-desorption isotherms of the investigated samples using ethanol as a prope solvent, shown in Figure 6S, was used to confirm the subtle change in molecular order as a response to $\Delta T_{S:AS}$ alteration. Pure drug NPs (F1, F3 and F5) were crystallising at 70% partial pressure (p/p_0) of ethanolic vapour, while those stabilised with P407 (F2, F4 and F6) were found to crystallise at 50% p/p_0. The enthalpies of melting obtained from the DSC

analysis (Figure 2S), suggest that the change in the P407 content with antisolvent temperature was not statistically significant, 6.76±1.15% at T_{AS}=0.5 °C (F2), 6.43±0.37 (F4) at T_{AS}=50 °C, and 5.19±0.99 (F6) T_{AS}=80 °C and indicates a relatively high drug loading in these samples. Crystallisation of ITR NPs at lower p/p_0 of ethanolic vapour when a hydrophilic polymer is included has been reported by our group before [4]. Here, crystallisation of NPs at those low p/p_0 values is not only due to the hydrophilic nature of the polymer included, but also due to its known effect of inducing crystallisation of ITR via increasing molecular mobility [3]. The change in the degree of disorder of NPs with the change in $\Delta T_{S:AS}$ compared to $\Delta T_{S:AS}$=0 °C has been calculated using Eq S1. In case of pure drug NPs, there was a statistically significant increase in the degree of disorder as the $\Delta T_{S:AS}$ increased, 5.39 ± 0.6 and 2.22 ± 0.9% for $\Delta T_{S:AS}$=49.5 and 30 °C, respectively, compared to $\Delta T_{S:AS}$=0 °C. The maximum disorder was observed when $\Delta T_{S:AS}$=49.5 °C. This increase in the degree of disorder with larger $\Delta T_{S:AS}$ was higher when P407 was included (18.6±0.3 and 13.5±7 % for $\Delta T_{S:AS}$=49.5 and 30 °C, respectively), which is consistent with the WAXS results. SEM investigations of post DVS powder (Figure 6Sc and d) revealed that NPs crystallised individually to form nanocrystalline aggregates, which had the same diffraction peaks as the starting material when examined using WAXS.

DVS moisture isotherm of a full cycle of sorption-desorption of the nematic (F1) and smectic (F3) are displayed in figure 8. The isotherms revealed that, at 90% RH, the nematic LC NPs sorbed slightly more water (2.49±0.03 %) compared to their smectic counterparts (2.38±0.01) which indicate higher permeability of the nematic NPs. Hysteresis was observed in both isotherms, where the water content at each relative humidity point is higher in the desorption than sorption [4].

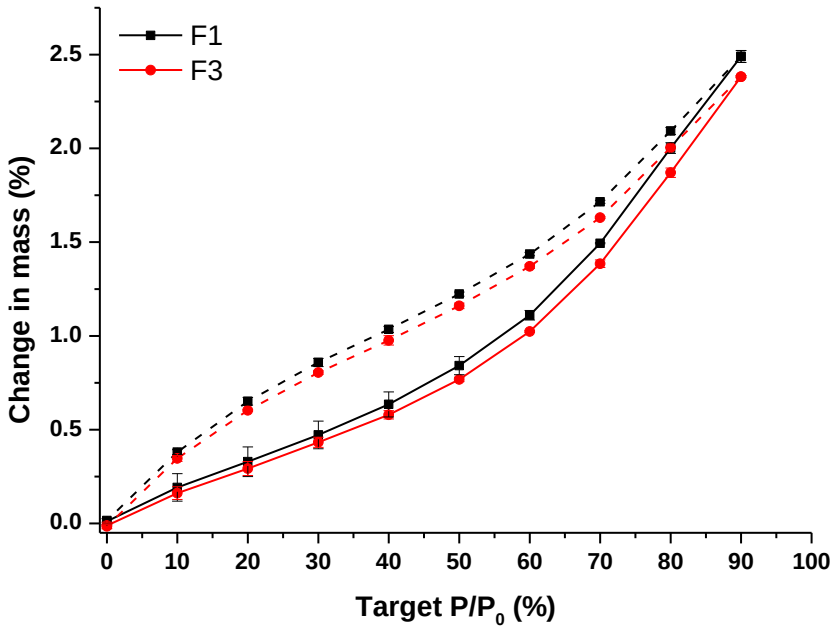

Figure 8. DVS moisture sorption-desorption isotherm of nematic (F1) and smectic (F3) LC NPs. Solid line representing sorption cycle while dashed line representing desorption cycle.

The absence of a sharp mass loss in both isotherms, similar to those observed in figure 6S, excludes the presence of any crystallization and indicate that the LC NPs are stable under the investigated conditions.

4. Conclusions

An investigation of the factors governing the quasi nanoemulsion precipitation of ITR revealed the ability to tune the properties of the produced nanoparticles/nanoaggregates via controlling the fabrication conditions. The higher the temperature difference between the solvent and antisolvent phases ($\Delta T_{S:AS}$), the thinner the particle shell thickness and the lower the molecular order with the nematic LC phase arrangement. The highest periodically ordered intercalated SmA mesosphere was observed when $\Delta T_{S:AS}$=0 °C with the inclusion of P407 in the antisolvent phase. Similarly, at a given temperature, the higher the solvent to antisolvent viscosity ratio, the smaller the nanoparticles produced. The ability to prepare P407 stabilised ITR NPs, at an elevated temperature, was demonstrated here while was not

feasible before [13]. It should be highlighted that to date a liquid crystalline phase of ITR has been only achieved via melting followed by cooling and here we demonstrate the feasibility of the use of a precipitation technique to accomplish this and the ability to confine the obtained phase in the nanosphere. This comprehensive study might help in the rational design of NPs made of other drugs.

Acknowledgements

This work was supported by the Science Foundation Ireland under Grant No. 12/RC/2275 (Synthesis and Solid State Pharmaceuticals Centre). The authors would like to thank Dr. Grzegorz Garbacz (Physiolution GmbH, Germany) for kindly supplying ITR, Prof. Owen Corrigan for reading the manuscript and useful discussion, Dr. Karsten Fleischer (School of Physics, TCD) for performing SAXS, the BARDS team in UCC (Dr. Dara Fitzpatrik, Dr. Bastian Vos and Dr. Rachel Evans-Hurson) for sharing their knowledge on solvent interactions and Dr. Eoin K. McCarthy (CRANN, TCD) for performing TEM imaging.

References

1. Dressman, J. B.; Reppas, C. In vitro-in vivo correlations for lipophilic, poorly water-soluble drugs. *Eur J Pharm Sci* **2000,** *11*, S73-S80.
2. Miller, M. A.; DiNunzio, J.; Matteucci, M. E.; Ludher, B. S.; Williams, R. O.; Johnston, K. P. Flocculated amorphous itraconazole nanoparticles for enhanced in vitro supersaturation and in vivo bioavailability. *Drug development and industrial pharmacy* **2012,** *38* (5), 557-70.
3. Matteucci, M. E.; Paguio, J. C.; Miller, M. A.; Williams, R. O.; Johnston, K. P. Flocculated amorphous nanoparticles for highly supersaturated solutions. *Pharmaceutical research* **2008,** *25* (11), 2477-2487.
4. Mugheirbi, N. A.; Paluch, K. J.; Tajber, L. Heat induced evaporative antisolvent nanoprecipitation (HIEAN) of itraconazole. *International journal of pharmaceutics* **2014,** *471* (1-2), 400-411.
5. Mapesa, E. U.; Tarnacka, M.; Kaminska, E.; Adrjanowicz, K.; Dulski, M.; Kossack, W.; Tress, M.; Kipnusu, W. K.; Kaminski, K.; Kremer, F. Molecular dynamics of itraconazole confined in thin supported layers. *Rsc Adv* **2014,** *4* (54), 28432-28438.
6. Su, Z. The investigation of pharmaceutical liquid crystals: Formation, stability and phase behavior. The investigation of pharmaceutical liquid crystals: Formation, stability and phase behavior, Purdue University, 2011.
7. Bisoyi, H. K.; Kumar, S. Liquid-crystal nanoscience: an emerging avenue of soft self-assembly. *Chem Soc Rev* **2011,** *40* (1), 306-319.
8. Tanaka, D.; Ishiguro, H.; Shimizu, Y.; Uchida, K. Thermal and photoinduced liquid crystalline phase transitions with a rod-disc alternative change in the molecular shape. *J Mater Chem* **2012,** *22* (48), 25065-25071.

9. Liversidge, G. G.; Cundy, K. C. Particle-Size Reduction for Improvement of Oral Bioavailability of Hydrophobic Drugs .1. Absolute Oral Bioavailability of Nanocrystalline Danazol in Beagle Dogs. *International journal of pharmaceutics* **1995,** *125* (1), 91-97.
10. Six, K.; Verreck, G.; Peeters, J.; Binnemans, K.; Berghmans, H.; Augustijns, P.; Kinget, R.; Van den Mooter, G. Investigation of thermal properties of glassy itraconazole: identification of a monotropic mesophase. *Thermochim Acta* **2001,** *376* (2), 175-181.
11. Sarnes, A.; Kovalainen, M.; Hakkinen, M. R.; Laaksonen, T.; Laru, J.; Kiesvaara, J.; Ilkka, J.; Oksala, O.; Ronkko, S.; Jarvinen, K.; Hirvonen, J.; Peltonen, L. Nanocrystal-based per-oral itraconazole delivery: Superior in vitro dissolution enhancement versus Sporanox (R) is not realized in in vivo drug absorption. *J Control Release* **2014,** *180*, 109-116.
12. Badawi, A. A.; El-Nabarawi, M. A.; El-Setouhy, D. A.; Alsammit, S. A. Formulation and Stability Testing of Itraconazole Crystalline Nanoparticles. *Aaps Pharmscitech* **2011,** *12* (3), 811-820.
13. Matteucci, M. E.; Hotze, M. A.; Johnston, K. P.; Williams, R. O. Drug nanoparticles by antisolvent precipitation: Mixing energy versus surfactant stabilization. *Langmuir : the ACS journal of surfaces and colloids* **2006,** *22* (21), 8951-8959.
14. Thakral, S.; Thakral, N. K. Prediction of drug-polymer miscibility through the use of solubility parameter based flory-huggins interaction parameter and the experimental validation: PEG as model polymer. *Journal of pharmaceutical sciences* **2013,** *102* (7), 2254-2263.
15. Umerska, A.; Paluch, K. J.; Inkielewicz-Stepniak, I.; Santos-Martinez, M. J.; Corrigan, O. I.; Medina, C.; Tajber, L. Exploring the assembly process and properties of novel crosslinker-free hyaluronate-based polyelectrolyte complex nanocarriers. *International journal of pharmaceutics* **2012,** *436* (1-2), 75-87.
16. Wang, X.; Gillian, J. M.; Kirwan, D. J. Quasi-emulsion precipitation of pharmaceuticals. 1. Conditions for formation and crystal nucleation and growth behavior. *Cryst Growth Des* **2006,** *6* (10), 2214-2227.
17. Arca, E.; Fleischer, K.; Krasnikov, S. A.; Shvets, I. Effect of Chemical Precursors On the Optical and Electrical Properties of p-Type Transparent Conducting Cr2O3:(Mg,N). *J Phys Chem C* **2013,** *117* (42), 21901-21907.
18. Wood, P. A.; Olsson, T. S. G.; Cole, J. C.; Cottrell, S. J.; Feeder, N.; Galek, P. T. A.; Groom, C. R.; Pidcock, E. Evaluation of molecular crystal structures using Full Interaction Maps. *Crystengcomm* **2013,** *15* (1), 65-72.
19. Higuchi, T., Connoras K.A. Phase solubility techniques. *Adv Anal Chem Instrum* **1965,** *4*, 117-210.
20. Sun, W.; Mao, S.; Shi, Y.; Li, L. C.; Fang, L. Nanonization of itraconazole by high pressure homogenization: stabilizer optimization and effect of particle size on oral absorption. *Journal of pharmaceutical sciences* **2011,** *100* (8), 3365-73.
21. Studart, A. R.; Amstad, E.; Gauckler, L. J. Colloidal stabilization of nanoparticles in concentrated suspensions. *Langmuir : the ACS journal of surfaces and colloids* **2007,** *23* (3), 1081-90.
22. Vandervoort, J.; Ludwig, A. Biocompatible stabilizers in the preparation of PLGA nanoparticles: a factorial design study. *International journal of pharmaceutics* **2002,** *238* (1-2), 77-92.
23. Ketelson, H. A.; Pelton, R.; Brook, M. A. Colloidal stability of Stober silica in acetone-water mixtures. *Journal of colloid and interface science* **1996,** *179* (2), 600-607.
24. Voorhees, P. W. The Theory of Ostwald Ripening. *J Stat Phys* **1985,** *38* (1-2), 231-252.
25. Li, D. X.; He, Q.; Yang, Y.; Mohwald, H.; Li, J. B. Two-stage pH response of poly(4-vinylpyridine) grafted gold nanoparticles. *Macromolecules* **2008,** *41* (19), 7254-7256.
26. Takeuchi, H.; Matsui, Y.; Yamamoto, H.; Kawashima, Y. Mucoadhesive properties of carbopol or chitosan-coated liposomes and their effectiveness in the oral administration of calcitonin to rats. *J Control Release* **2003,** *86* (2-3), 235-242.
27. DiNunzio, J. C.; Miller, D. A.; Yang, W.; McGinity, J. W.; Williams, R. O. Amorphous Compositions Using Concentration Enhancing Polymers for Improved Bioavailability of Itraconazole. *Molecular pharmaceutics* **2008,** *5* (6), 968-980.

28. Kachrimanis, K.; Ktistis, G.; Malamataris, S. Crystallisation conditions and physicomechanical properties of ibuprofen-Eudragit (R) S100 spherical crystal agglomerates prepared by the solvent-change technique. *International journal of pharmaceutics* **1998,** *173* (1-2), 61-74.
29. Cui, F. D.; Yang, M. S.; Jiang, Y. Y.; Cun, D. M.; Lin, W. H.; Fan, Y. L.; Kawashima, Y. Design of sustained-release nitrendipine microspheres having solid dispersion structure by quasi-emulsion solvent diffusion method. *J Control Release* **2003,** *91* (3), 375-384.
30. Nocent, M.; Bertocchi, L.; Espitalier, F.; Baron, M.; Couarraze, G. Definition of a solvent system for spherical crystallization of salbutamol sulfate by quasi-emulsion solvent diffusion (QESD) method. *Journal of pharmaceutical sciences* **2001,** *90* (10), 1620-1627.
31. Re, M. I.; Biscans, B. Preparation of microspheres of ketoprofen with acrylic polymers by a quasi-emulsion solvent diffusion method. *Powder Technol* **1999,** *101* (2), 120-133.
32. Yang, M. S.; Cui, F. D.; You, B. G.; Fan, Y. L.; Wang, L.; Yue, P.; Yang, H. Preparation of sustained-release nitrendipine microspheres with Eudragit RS and Aerosil using quasi-emulsion solvent diffusion method. *International journal of pharmaceutics* **2003,** *259* (1-2), 103-113.
33. Karam, H. J. a. B., J.C. Deformation and breakup of liquid droplets in a simple shear field. *I & EC Fundamentals* **1968,** *7* (4), 6.
34. Wang, X.; Kirwan, D. J. Quasi-emulsion precipitation of pharmaceuticals. 2. Application to control of polymorphism. *Cryst Growth Des* **2006,** *6* (10), 2228-2240.
35. Espitalier, F.; Biscans, B.; Laguerie, C. Particle design Part A: Nucleation kinetics of ketoprofen. *Chemical Engineering Journal* **1997,** *68* (2-3), 95-102.
36. Wiebe, R., Gaddy, V.L. The solubility of carbon dioxide in water at various temperatures from 12 to 40° and at pressures to 500 atm. *J. Am. Chem. Soc.* **1940,** *62*, 815–817.
37. Espitalier, F.; Biscans, B.; Laguerie, C. Particle design Part B: batch quasi-emulsion process and mechanism of grain formation of ketoprofen. *Chemical Engineering Journal* **1997,** *68* (2-3), 103-114.
38. Chen, X.; Benhayoune, Z.; Williams, R. O.; Johnston, K. P. Rapid dissolution of high potency itraconazole particles produced by evaporative precipitation into aqueous solution. *J Drug Deliv Sci Tec* **2004,** *14* (4), 299-304.
39. Tarnacka, M.; Adrjanowicz, K.; Kaminska, E.; Kaminski, K.; Grzybowska, K.; Kolodziejczyk, K.; Wlodarczyk, P.; Hawelek, L.; Garbacz, G.; Kocot, A.; Paluch, M. Molecular dynamics of itraconazole at ambient and high pressure. *Physical Chemistry Chemical Physics* **2013,** *15* (47), 20742-20752.
40. Zeng, X. B.; Ungar, G.; Liu, Y. S.; Percec, V.; Dulcey, S. E.; Hobbs, J. K. Supramolecular dendritic liquid quasicrystals. *Nature* **2004,** *428* (6979), 157-160.
41. Domenici, V. Order and dynamics of rod-like and banana-shaped liquid crystals by H-2 NMR. *Pure Appl Chem* **2007,** *79* (1), 21-37.
42. D. Demus, J. G., G.W. Gray, H.W. Spiess, V. Vill. *Handbook of Liquid Crystals: Fundamentals*; Wiley-VCH: Weinheim, 1998; Vol. 1.
43. Mcmillan, W. L. X-Ray Scattering from Liquid-Crystals .1. Cholesteryl Nonanoate and Myristate. *Phys Rev a-Gen Phys* **1972,** *6* (3), 936-+.
44. Davey, R. J.; Garside, J.; Hilton, A. M.; Mcewan, D.; Morrison, J. W. Purification of Molecular Mixtures Below the Eutectic by Emulsion Crystallization. *Nature* **1995,** *375* (6533), 664-666.
45. Kaminska, E.; Tarnacka, M.; Kolodziejczyk, K.; Dulski, M.; Zakowiecki, D.; Hawelek, L.; Adrjanowicz, K.; Zych, M.; Garbacz, G.; Kaminski, K. Impact of low molecular weight excipient octaacetylmaltose on the liquid crystalline ordering and molecular dynamics in the supercooled liquid and glassy state of itraconazole. *European Journal of Pharmaceutics and Biopharmaceutics* **2014,** *88* (3), 1094-1104.
46. Nonappa; Lahtinen, M.; Kolehmainen, E.; Haarala, J.; Shevchenko, A. Evidence of Weak Halogen Bonding: New Insights on Itraconazole and its Succinic Acid Cocrystal. *Cryst Growth Des* **2013,** *13* (1), 346-351.
47. Cyr, T. D.; Dawson, B. A.; Neville, G. A.; Shurvell, H. F. Spectral characterization of fluconazole. *Journal of pharmaceutical and biomedical analysis* **1996,** *14* (3), 247-255.

692